Midinfrared properties of cuprous oxide: High-order lattice vibrations and intraexcitonic transitions of the 1*s* paraexciton

M. Jörger,* T. Fleck, and C. Klingshirn
Institut für Angewandte Physik, Universität Karlsruhe, D-76128 Karlsruhe, Germany

R. von Baltz
Institut für Theorie der Kondensierten Materie, Universität Karlsruhe, D-76128 Karlsruhe, Germany
(Received 12 November 2004; published 30 June 2005)

This contribution addresses both the general mid-infrared (MIR) properties of Cu_2O and induced absorption due to intraexcitonic $1s \rightarrow 2p$ transitions under simultaneous cw laser excitation. After an overview of the current state of knowledge and remaining open questions concerning excitons in Cu_2O we will first discuss several absorption bands in the spectral range between approximately 100 and 150 meV in terms of multiphonon and biphonon features. The second, more extensive part will concern a pump-probe experiment in the limit of low densities of 1*s* excitons where we investigated intraexcitonic transitions appearing in the MIR spectral range as well. We find a signal which can be clearly assigned to a 1*s para* $\rightarrow$ 2*p para* transition and present various data depending on excitation conditions and sample temperature. Applying the results of detailed theoretical considerations we can estimate the density and lifetime of the 1*s para*-exciton and at least speculate about its dispersion.

DOI: 10.1103/PhysRevB.71.235210 PACS number(s): 71.35.−y

I. INTRODUCTION AND CURRENT STATE OF KNOWLEDGE

The excitonic system of the dipole forbidden, direct band gap semiconductor cuprous oxide (Cu_2O) qualifies as unique in many respects. Its beautiful series of *np* excitons,[1] where *n* is the main quantum number and *p* describes states with an angular momentum of $\ell = 1$, is matchless within semiconductor physics. Since the energies of these *p*-like excitons perfectly fulfill the $1/n^2$ relation known from atomic hydrogen, the appearance of this so-called yellow series impressively emphasizes the quantum mechanical analogy between excitons and atoms. Though these properties are well-known since approximately 50 years,[2] excitons in Cu_2O are still a matter of current research, mainly due to the special features of the 1*s* state. While the excitons with $n \geqslant 2$ are pure Wannier states as the extent of their wave function is large compared to the volume of one unit cell, this is no more true for the 1*s* state: since its excitonic Bohr radius ($a_{1s} \approx 0.53$ nm) (Ref. 3) is comparable to the lattice constant ($a_l \approx 0.43$ nm),[4] the so-called central cell corrections[3] result in significant deviations. First, the 1*s* exciton is considerably split by electron hole exchange interaction into the triply degenerate 1*s ortho*-exciton (total angular momentum $J=1$) and the 1*s para*-exciton ($J=0$), lying 12 meV lower in energy.[5] Second, reduced Coulomb screening gives rise to an increased binding energy ($E_{B,1s\text{-}para} \approx 151$ meV, $E_{B,1s\text{-}ortho} \approx 139$ meV),[5] leading to a substantial deviation of the 1*s* energy from the afore mentioned $1/n^2$ relation. Lastly, because the small extent in real space corresponds to a rather large one in momentum space, also the effective mass is affected. The contribution of nonzone center areas of the Brillouin zone, where valence and conduction band already flatten, leads to an increase of the effective 1*s* mass.[3] While the effective mass of the *np* excitons ($m_{np} \approx 1.68 m_0$, m_0=free electron mass)[6] is just given by the sum of effective electron and hole masses, it has been determined to be $m_{1s} \approx 2.7 m_0$ for the 1*s ortho*-exciton.[7] In this regard there is a lack of experimental data for the 1*s para*-exciton, which is up to now expected to have an identical effective mass.

Due to the inversion symmetric crystal structure of Cu_2O, parity is a good quantum number and thus both 1*s* species are dipole forbidden. While the 1*s ortho*-exciton is quadrupole allowed, the 1*s para*-exciton is optically one-photon forbidden in all orders of perturbation theory. Apart from one emission line of almost negligible efficiency,[8] the 1*s para*-exciton is also unable to decay via phonon assisted luminescence. Disregarding high density effects, the two dominant loss mechanisms are impurity recombination and phonon assisted conversion into 1*s ortho*-excitons.[9] Since especially at low temperatures ($T < 30$ K) both of these mechanisms are rather slow, this implies a long lifetime. Unfortunately the same reasons giving rise to this long lifetime, make the 1*s para*-exciton hardly traceable as well. This dilemma is emphasized by different published lifetimes such as 20 ns,[10] 13 μs,[11] 3 ms,[12] and 14 ms (Ref. 13) stretching across more than five orders of magnitude.

Due to their high Mott density ($n_{\mathrm{Mott}} > 10^{21}/\mathrm{cm}^3$) where a transition to an electron hole plasma should take place, 1*s* excitons in Cu_2O are considered to be promising candidates for the observation of excitonic Bose-Einstein condensation (BEC) since more than two decades.[14] Owing to both, its long lifetime and the absence of the polariton effect which could otherwise prevent a condensation to $\mathbf{k}=0$, in particular the 1*s para*-exciton bears good prospects to exhibit this phase transition. Many efforts have been made[15,16] but none of them were generally accepted as a proof of excitonic BEC. Again this dissatisfactory state of affairs mainly arises from the lack of a reliable means of detection for 1*s para*-excitons, including their energetical distribution.

In a recent theoretical work[17] Johnson and Kavoulakis proposed an alternative method to detect 1*s* excitons in Cu_2O. Instead of interband spectroscopy the authors suggested to use intraexcitonic 1*s* to 2*p* transitions which are dipole allowed for both of the 1*s* species. Furthermore they showed that due to the different effective masses of 1*s* and 2*p* excitons, the line shape of these transitions should provide valuable information about the energetical distribution of the 1*s* excitons. Consulting once again the analogy between excitons and atoms, the entirety of all 1*s* to *np* transitions is nothing else but the excitonic version of the Lyman series, well-known from atomic hydrogen. Experimentally, indeed such measurements are by far more challenging than their counterpart in atomic physics. Depending on initial and final state, the nominal transition energies are situated in the MIR spectral range between 115 meV and 151 meV. In order to probe the transitions, the initial state namely the 1*s* exciton has to be populated by external laser excitation, thus requiring a differential absorption experiment. This rather modern kind of combined visible and infrared pump-probe spectroscopy is nowadays often referred to as terahertz spectroscopy. It was first applied to silicon[18] and germanium[19] since in these indirect semiconductors already moderate excitation creates sufficiently high densities due to the long exciton lifetimes.

The main part of this contribution will focus on intraexcitonic 1*s* to 2*p* transitions in Cu_2O in the limit of low exciton densities ($\leqslant 10^{14}/cm^3$), created by moderate cw-laser excitation. First attempts[20] where we found both broad and narrow induced absorption bands in the spectral regions of $1s \rightarrow 2p$ *para* and *ortho*-exciton transitions, respectively, but which might have been caused according to our present results (see Sec. IV D) at least partly by transitions of impurity bound excitons, prompted us to improve the infrared signal to noise ratio by more than one order of magnitude. Indeed this was essential since the actual induced 1*s* to 2*p* absorption signal turned out to be much weaker than we originally expected. As will be shown, the signal considerably deviates from the predictions based on a simple model already in the low density limit. Therefore the comprehension of this low density signal is a required precondition for the investigation of its high density behavior.

An important work closely related to ours, has been recently published by Kuwata-Gonokami *et al.*[21] In a time-resolved high density experiment 1*s* to 2*p* transitions of both *ortho*- and *para*-excitons were observed unambiguously within the first 400 ps after short pulse excitation (FWHM ≈ 150 fs). The authors estimate the 1*s* density to be in the order of $10^{15}/cm^3$ but as we will show later, it could be rather one order of magnitude higher. While we totally agree with the experimental findings of Ref. 21 we will sometimes also point out where we partly disagree with the given interpretation. It will emerge that the data of our contribution and Ref. 21 complete one another: their combination, based on a more sophisticated density calibration, yields important information such as the lifetime of the 1*s* *para*-exciton and the creation efficiency of 1*s* excitons in Cu_2O. Beyond we will accomplish a detailed line shape analysis and also present various data as a function of excitation conditions and temperature.

This work is organized as follows: in Sec. II the experimental setup as well as the employed set of samples are described. Section III addresses the general mid-infrared (MIR) properties of Cu_2O in the range between approximately 90 meV and 160 meV. In order to judge the accuracy of the pump-probe experiment, all samples were characterized in the spectral region of interest, yielding temperature dependent data of various absorption bands. Although the assignment of these features is partly ambiguous, we consider it important to include these findings as well, since such quantitative and spectrally high resolved data have not been published hitherto and since we need the temperature dependence of theses features as a "thermometer" for the lattice temperature under excitation. In Sec. IV the results of the 1*s* to 2*p* terahertz transitions will be presented and discussed in detail. For the purpose of a better readability we decided to derive the required theoretical relations directly where they are needed for discussion and interpretation of the experimental results.

II. EXPERIMENTAL SETUP

A. Employed samples

The measurements were carried out with seven samples of various thicknesses between 210 μm and 3 mm, fabricated from three different naturally grown crystals of high quality. The main surfaces of five of the investigated samples were (111) planes, those of the remaining two were (110) respectively (100) planes.

Since the most prominent MIR absorption band is rather strong, the thinnest sample of 210 μm was particularly suitable for general MIR characterization. Concerning the ideal thickness for the pump-probe experiment, a compromise had to be found. A sample which is too thin involves two disadvantages: first the exciton density might be reduced by enhanced surface recombination and secondly multiple reflections reduce the MIR signal to noise ratio. On the other hand, if the sample is too thick, the transmitted MIR intensity becomes too weak, resulting in a reduced sensitivity for the excitation induced transitions as well. In this context samples ranging between 600 μm and 1 mm turned out to be ideal for the applied experimental setup. The samples were mounted as strainfree as possible using a special grease (APIEZON N) of high heat conductivity, which may according to the manufacturer even have a bit of flexibility left at liquid helium temperature.

B. Linear and differential absorption measurements

The MIR characterization as well as the induced absorption experiment were accomplished with a Bruker IFS113v Fourier transform spectrometer. In both cases the unpolarized MIR beam was focused perpendicularly on a sample area of approximately 3 mm^2. As a MIR source we applied a globar the emission characteristics of which approximately correspond to a black body radiator with a temperature of $T \approx 1450$ K. The transmitted MIR signal was detected by a liquid nitrogen cooled mercury cadmium telluride (MCT) detector. In order to avoid problems caused by atmospheric

absorption lines, the whole MIR path of rays was evacuated to a pressure well below 1 mbar. The spectral resolution for all of the presented measurements was approximately 30 μeV.

Since it is about standard absorption spectroscopy, we do not go into detail concerning the general MIR characterization but focus on the particularities of the pump-probe setup. The sample could alternatively be excited by a tunable cw dye laser (photon energy $E_\gamma \approx 2.06$ eV ± 50 meV) either resonantly in the 1*s ortho*-excitons quadrupole resonance or in its phonon assisted absorption continuum, as well as above the band gap by using a cw Verdi laser ($E_\gamma \approx 2.33$ eV). Since the laser had to be launched into the spectrometer from outside, geometrical reasons made a small angle of approximately 10° between pump- and probe-beam inevitable. To avoid artefacts due to transmitted or scattered laserlight either on the detector or on the interferometer beamsplitter, we attached two appropriate germanium filters showing no MIR differential absorption signal themselves.

Compared to pulsed excitation experiments such as those in Ref. 21 with a moderate repetition rate of 1 kHz, the average amount of heat generated inside the cryostat by cw excitation can be distinctly higher, thus requiring additional precautions. Due to the finite distance between sample and sensor, the displayed temperature under simultaneous laser excitation is not reliable anymore since a temperature gradient develops. Although the MIR absorption bands presented in Sec. III seem to have a rather unfavorable influence on the pump-probe experiment, their temperature sensitivity perfectly serves for an accurate temperature calibration under simultaneous laser excitation. Dividing two transmission spectra by each other, one with and one without laser excitation, already temperature differences well below 1 K lead to a characteristic tilt of the resulting ratio.

In standard Fourier transform spectroscopy the sample is usually placed inside the isolation vacuum of a continuous flow cryostat, allowing for heat dissipation only by the contact area between sample and sampleholder. Using the aforementioned calibration method it turned out that this standard cryostat fails to reach sample temperatures below approximately 100 K for typically absorbed excitation powers of several 100 mW. Therefore we developed a special pump-probe cryostat, optimized for efficient heat dissipation. Although the limited amount of space in the spectrometer volume still constrained us to adopt the flow cryostat principle, it was possible to meet the requirements and to reach sample temperatures down to 10 K for absorbed excitation powers up to 400 mW. By placing the sample directly in the helium flow, the helium acts as both, contact gas and medium to transport heat efficiently away via the pump connections. Summing over all sources of error even a conservative guess results in a maximum error bar of $\Delta T \approx 2$ K for the pump-probe results in Sec. IV.

III. MEASUREMENTS WITHOUT PUMP

A. Survey of the MIR absorption bands

Figure 1 gives an overview of the MIR features of Cu_2O which can all be clearly assigned to absorption since they scale with sample thickness. The spectrum can be phenomenologically divided into two main bands (1 and 2) as well as three sidebands (1b, 1c, and 2b) which were observed on all samples and showed no clear dependence on either the samples orientation or the crystal it was fabricated from. The small shoulder at 139 meV is too difficult to deconvolute from the main band 2 and is therefore not considered in the following. At higher photon energies between 160 meV and $\approx$500 meV all samples were rather transparent, showing no pronounced absorption features. Regarding the pump-probe experiment it was particularly the temperature dependence of band 2 and 2b which turned out to be an ideal "thermometer" for the real sample temperature under simultaneous laser excitation.

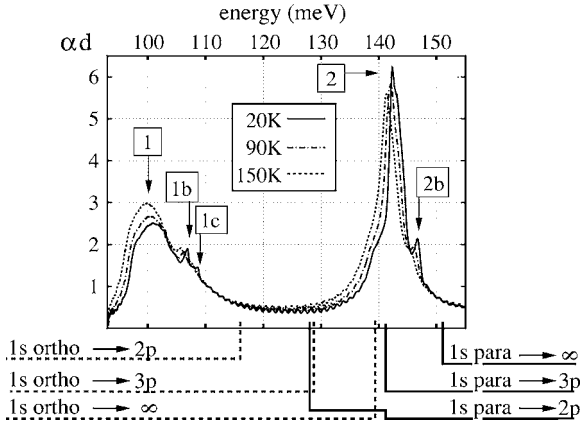

FIG. 1. Temperature dependent MIR optical density αd of a 210 μm thick (111) sample. With regard to the pump-probe experiment a subset of the nominal 1*s* to *np* transition energies for $T = 10$ K is indicated as well, whereas transitions to ∞ describe the ionization of the corresponding 1*s* exciton.

B. Biphonons, multiphonons, and localized phononmodes

After some preliminary remarks about fundamental optical phonon modes, we will review the proximate candidates to explain the observed MIR bands, namely biphonons, multiphonons, and localized phonon modes. For the explanation of these terms see below. Since its unit cell contains 6 atoms, Cu_2O possesses 15 optical phonon-branches[22,23] which are reduced to 8 branches at the Γ-point by degeneracy.[5,24] Especially regarding the four high energy zone center modes ($E \geqslant 40$ meV) the published energies vary by several meV. Depending on the particular phonon mode, the bandwidth of the branches in **k**-space ranges between approximately 1 meV and 20 meV.[22,23]

The concept of biphonons as a fundamental excitation with a defined wave vector **k** was introduced by Agranovich[25] and describes the bound state of two phonons. The attractive phonon-phonon interaction necessary for the formation of this quasiparticle implies finite nonharmonic contributions to the lattice potential. The biphonon energy is given by the sum of the energies of the constituting phonons $[E_1(\mathbf{k}_1), E_2(\mathbf{k}_2)]$ reduced by the binding energy $E_B(\mathbf{k})$,

$$E(\mathbf{k}) = E_1(\mathbf{k}_1) + E_2(\mathbf{k}_2) - E_B(\mathbf{k}), \quad \mathbf{k} = \mathbf{k}_1 + \mathbf{k}_2. \qquad (1)$$

Unlike biphonons, so-called multiphonons concern a linear superposition of phonons and thus a many particle excitation.

In the simplest case two phonons of the same branch and with same frequency ω are simultaneously created by infrared excitation, resulting in an absorption peak at the overtone energy $E=2\hbar\omega$. In general, several phonons of different branches i can be either created or annihilated[26] with a total multiphonon energy of

$$E(\mathbf{k}_1,\mathbf{k}_2,\ldots)=\sum_i n_i E_i(\mathbf{k}_i), \quad n_i \in \mathbb{Z}. \tag{2}$$

Processes where phonons are solely created ($n_i \geqslant 0$) are called summation processes, if phonons are annihilated as well they are referred to as confluence processes.[26]

Since we are dealing with infrared absorption, momentum conservation implies $\Sigma_i n_i \mathbf{k}_i \approx 0$ for multiphonons, respectively, $\mathbf{k}\approx 0$ for biphonons. However as can be seen in Eqs. (1) and (2), phonons from the whole Brillouin zone can contribute. Still having in mind the number and bandwidth of the different branches as well as the error bar of the high energy modes, it is clear that an assignment of the MIR absorption bands in terms of biphonons or multiphonons must remain at least partly ambiguous. The multiphonon dipole as well as quadrupole selection rules for the most simple case of binary combinations in a perfect Cu_2O crystal are given in Ref. 27. Accounting for all points of high symmetry in **k**-space, already in dipole approximation there are more than 30 allowed binary combinations, increasing to a total of 89 binary combinations including quadrupole order.

In reality the Cu_2O crystals are not perfect but contain defect densities ranging between 10^{15} and $10^{18}/\mathrm{cm}^3$.[28–30] Several authors[31–33] point out that therefore local inversion and translation symmetry might be destroyed, leading to a breakdown of multiphonon selection rules. As a consequence no multiphonon combination may be strictly excluded and selection rules can at best be quoted as subsidiary arguments for possible binary combinations. In order to keep the discussion manageable however, we make two additional assumptions. First, since the absorption bands were already observed at low temperatures ($T=10$ K), we only allow for multiphonon summation processes. Secondly, assuming that such processes are more likely, we will favor combinations of preferably low order.

Another possibility is the formation of localized phonon modes[34] in the vicinity of point defects. Since with increasing distance from the defect their amplitude is rapidly damped, these modes cannot propagate through the crystal as plane waves. Especially if a localized phonon mode is unable to decay into fundamental modes it may result in an additional absorption band. In principle none of the observed MIR bands can strictly be excluded to stem from a localized phonon mode without a theoretical approach the predictions of which can experimentally be inspected. However we consider this less likely since none of the bands shows any dependence on the origin of the crystal it was measured in.

C. Absorption band at 100 meV

Since the maximum of band 1 is rather broad and less pronounced, its temperature dependent position cannot be extracted accurately enough to clarify its origin. Nevertheless

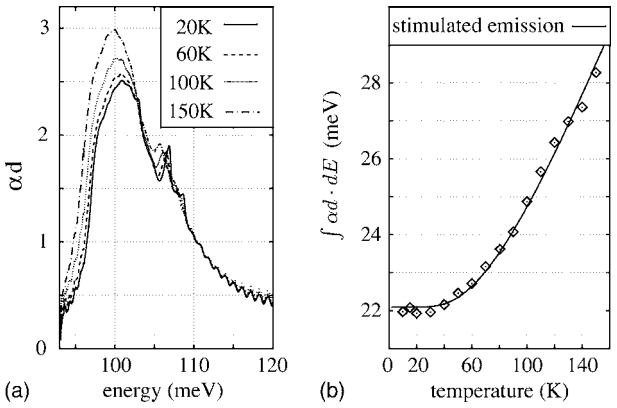

FIG. 2. (a) Absorption band 1 for various temperatures, measured on a 210 μm thick (111) sample. (b) The corresponding area $\int \alpha d \cdot dE$ as a function of temperature where the reflection offset as well as the influence of the sidebands 1b and 1c were removed. The solid line shows a fit according to Eq. (3) resulting in $E_i \approx 19.2$ meV.

we can make use of another feature: as can be seen in Fig. 2 the optical density of band 1 considerably increases with increasing temperature. While a biphonon band should become weaker due to enhanced thermal dissociation[35] the observed increase can be understood in terms of a multiphonon along with stimulated emission. Since phonons are bosons with a chemical potential $\mu=0$ in thermal equilibrium, their emission is proportional to $[1+f_B(E,T)]$ whereas $f_B(E,T)$ is the Bose-Einstein occupation probability. In the special case where apart from one phonon mode with the energy E_i all other contributing phonons fulfill $E \gg k_B T$, the multiphon intensity scales with temperature as

$$I(T)=\int \alpha(T) d \cdot dE = I_0 \left(1 + \frac{1}{\exp\left(\frac{E_i}{k_B T}\right)-1} \right). \tag{3}$$

As indicated by the solid line in Fig. 2(b), the integrated intensity of band 1 can be well reproduced according to Eq. (3), using a phonon energy of $E_i \approx 19.2$ meV.

A summary of the fundamental optical phonon modes at the Γ-point can, e.g., be found in Refs. 24 and 5. There are two pairs of zone center modes with symmetry Γ_{15}^- each of them split into a TO and a LO mode. The low energy pair is usually referred to as $\Gamma_{15}^{-(1)}$ (TO) and $\Gamma_{15}^{-(1)}$ (LO), while the high energy pair is labeled as $\Gamma_{15}^{-(2)}$ (TO) and $\Gamma_{15}^{-(2)}$ (LO). Since the extracted energy of 19.2 meV coincides well with the literature value of 19.1 meV ($T\approx 10$ K) for the $\Gamma_{15}^{-(1)}$ (LO) mode,[5,24,36] we propose that band 1 is associated with the phonon emission of the corresponding branch. Furthermore, a binary combination with the $\Gamma_{15}^{-(2)}$ (LO) branch, the published zone center energies of which range between 78.5 meV and 82.4 meV (Refs. 5 and 24) ($T\approx 10$ K), seems most probable and would be quadrupole allowed.[27] In addition the available dispersion data favors this combination over those including one or both of the corresponding TO modes. While the bandwidth of each TO mode is in the order of 1 meV,[23] it is approximately 10 meV (Ref. 22) for the

TABLE I. Nominal transition energies ΔE of dipole allowed intraexcitonic and interexcitonic transitions for $T \approx 10$ K. First block: intraexcitonic transitions within the yellow series (y) for neglected p level fine structure. 1s *ortho*$\rightarrow np$ energies are extracted from linear absorption and luminescence data, while 1s *para*$\rightarrow np$ energies are calculated by assuming a 1s splitting of 12 meV. Second block: interexcitonic transitions from the yellow 1s state to the green (Refs. 40–42) (g) and blue (Ref. 43) (b) series. Transitions to the indigo series are not included since they where outside the spectral range of the probe beam. Third block: intraexcitonic transitions within the green series.

Initial state	Series	Final state	Series	ΔE (meV)
1s *ortho*	y	2p *ortho*	y	115.6
1s *ortho*	y	3p *ortho*	y	128.5
1s *ortho*	y	$n=\infty$	y	139.1
1s *para*	y	2p *para*	y	127.6
1s *para*	y	3p *para*	y	140.5
1s *para*	y	$n=\infty$	y	151.1
1s *ortho*	y	2p *ortho*	g	235
1s *para*	y	2p *para*	g	247
1s *ortho*	y	1s *ortho*	b	547
1s *ortho*	g	2p *ortho*	g	130
1s *para*	g	2p *para*	g	141

$\Gamma_{15}^{-(1)}$ (LO) branch with a positive curvature at $\mathbf{k}=0$ and 5 meV (Ref. 23) for the $\Gamma_{15}^{-(2)}$ (LO) branch, but with a negative curvature. Assuming that phonons from the whole Brillouin zone contribute, the observed halfwidth of approximately 15 meV is in good agreement with the sum of the bandwidths of the $\Gamma_{15}^{-(1)}$ (LO) and $\Gamma_{15}^{-(2)}$ (LO) branches. Since even for the highest temperature of 150 K the $\Gamma_{15}^{-(2)}$ (LO) branch fulfills the condition $E \gg k_B T$, the corresponding stimulated emission term can be approximated by unity and the multiphonon intensity simply scales with the population of the low energy mode $\Gamma_{15}^{-(1)}$ (LO) via Eq. (3).

D. Absorption band at 142 meV

Because band 2 is the most striking MIR feature, the majority of the so far published MIR investigations concentrated on it along with different interpretations.[32,37] In Ref. 35 strong arguments based on temperature dependence support the conclusion that band 2 is of biphononic $2 \cdot \Gamma_{15}^{-(2)}$ (TO) origin. Therefore we will only discuss the influence of band 2 on the pump-probe experiment (Sec. IV).

Since the pump-probe samples are distinctly thicker, band 2 results in a detection gap of approximately 10 meV which covers some of the higher intraexcitonic transitions (compare Figs. 1 and 5) and Table I. Transitions accessible by differential absorption spectroscopy are with descending signal to noise ratio: 1s *para*$\rightarrow 2p$, 1s *ortho*$\rightarrow 3p$, 1s *ortho*$\rightarrow 2p$, 1s *para*$\rightarrow\infty$. The influence of this absorption peak and of that around 100 meV on the real part ε_1 of the MIR dielectric function can be shown to be of the order of 10^{-3}. Therefore

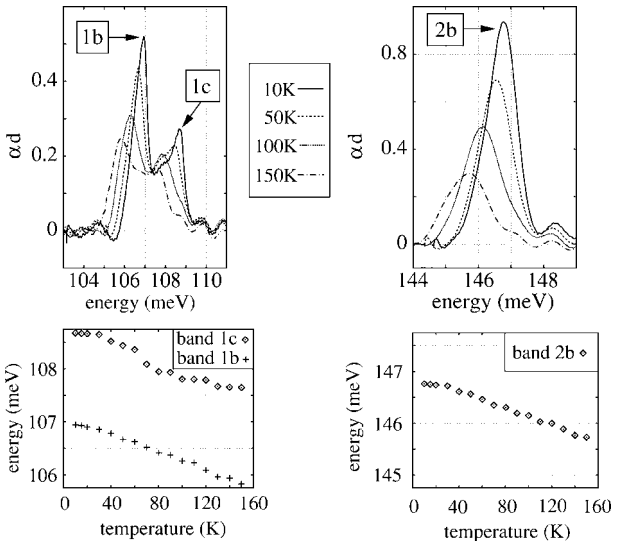

FIG. 3. **Upper left and upper right corner:** sidebands 1b, 1c, and 2b for various temperatures where the contribution of the main bands 1 and 2 was removed. **Lower left and lower right corner:** temperature dependent position of the absorption maximum of the different sidebands.

it is well justifiable to use the background dielectric constant[31] $\varepsilon_B \approx 6.5$ within the whole spectral range.

E. Sidebands at 147 meV, 109 meV, and 107 meV

Figure 3 shows the three sidebands 1b, 1c, and 2b sitting on top of the main bands 1 and 2, including their energetic position as a function of temperature. The data have been obtained by subtracting the temperature dependent main bands 1 and 2. These sidebands need not arise from the same processes as the main bands. We present in the following possible origins, however without being able to give a unique interpretation. Since their intensity decreases with increasing temperature one might argue that all three sidebands are due to biphonons. One way to distinguish between multiphonons and biphonons is the temperature dependent shift of the observed absorption band.[35] While a multiphonon shifts like the sum of all contributing fundamental modes, the theoretical temperature dependence of a biphonon is rather complicated and can, e.g., be found in Ref. 35. Using this approach and the temperature dependence of the fundamental modes from Refs. 24 and 35 does not allow us to reproduce our data in terms of a biphononic origin.

If the transition rate for multiphonon absorption is strongly $\mathbf{k}$-dependent, so that contributions from peculiar areas in the Brillouin zone dominate, then the intensities may also decrease with increasing temperature. Taking into account the multitude of possible combinations mentioned in Sec. III B and the phonon dispersion data and their temperature dependencies according to Refs. 5, 22–24, and 35 several adequate combinations can be found. However, the sum of the energies of zone center phonons alone tends for all proposed combinations to be too large compared to the data in Fig. 3. Consequently, contributions from other areas of the Brillouin zone must be involved. Since the splitting of bands

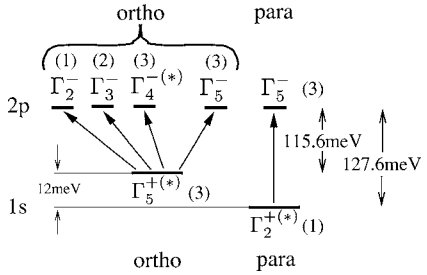

FIG. 4. Term diagram of the yellow series $1s$ and $2p$ states including the different irreducible representations with the corresponding degeneracies given in parentheses. States the energy of which is known from experiment are denoted with $(*)$. Dipole allowed transitions are indicated by arrows, whereas the energies on the right-hand side specify the nominal transition energies at $T=10$ K and neglected $2p$ fine structure.

1a and 1b is with 1.8 meV below the band width of most fundamental modes and since they shift parallel with temperature, one may argue that they result from the combination of the same phonon branches, but with contributions from different areas of **k**-space. Two ternary combinations would fit namely from the branches starting at Γ as $\Gamma_{15}^{-(2)} \times(\mathrm{TO})+2\cdot\Gamma_{15}^{-(1)}(\mathrm{LO})$ or $\Gamma_{15}^{-(2)}(\mathrm{LO})+2\cdot\Gamma_{15}^{-(1)}(\mathrm{TO})$. Sideband 2b may be explained by the simple binary combination $2\cdot\Gamma_{15}^{-(2)}$ (LO), implying that the contributing phonons are stemming from the M-point. Inclusion of localized phonon modes gives even more space for interpretation or speculation.

IV. MEASUREMENTS WITH PUMP

A. Selection rules and density calibration

Before presenting the results of the pump-probe experiment we first insert a theoretical section concerning intraexcitonic transitions. After a summary of selection rules and nominal transition energies we will focus on an exciton density calibration which is particularly important to determine the lifetime of the $1s$ *para*-exciton.

Due to spin-flip interdiction only transitions of the type $1s$ *ortho* $\rightarrow np$ *ortho* or $1s$ *para* $\rightarrow np$ *para* are strongly allowed. The term diagram of $1s$ and $2p$ states including the dipole allowed $1s\rightarrow 2p$ transitions is illustrated in Fig. 4. Actually the p-like excitons showing up in one photon absorption spectroscopy are only the subseries with symmetry Γ_4^- and all other remaining p states have never been experimentally observed.[38] With regard to $1s\rightarrow 2p$ transitions this implies that only the $2p$ *ortho* Γ_4^- energy is experimentally known and one could in principle expect fine structures. An estimation yields that possible splitting mechanisms should range on a sub-meV scale. Unlike the $1s$ state, for p-orbitals the probability of finding an electron and hole at the same place tends to zero and thus exchange interaction should be negligible. Corresponding to the hydrogen atom spin-orbit interaction can be estimated via[39] $E_B\cdot\alpha^2<10$ μeV where $E_B \approx 25$ meV is the $2p$ binding energy and $\alpha\approx 1/137$ is the Sommerfelds fine structure constant. Even with an appropriate spectral resolution it would be unlikely to observe such small fine structures since they should be covered by homogeneous broadening as will be shown in Sec. IV C.

Apart from intraexcitonic transitions within the yellow series there are two other transition types which might be of interest regarding the applied experimental setup. First, also interexcitonic transitions from the yellow series $1s$ states to excitons of the higher series[44] might appear. Besides spin-flip interdiction which is of course still valid, the dipole selection rules for interexcitonic transitions can be deduced from the symmetry of the involved valence and conduction bands. Secondly, in the case of excitation above the yellow band gap, green $1s$ excitons are created as well and thus intraexcitonic transitions within the green series cannot be excluded. Table I gives a summary of some nominal intraexcitonic as well as interexcitonic transition energies. In anticipation of the experimental results we already mention that we neither observed interexcitonic transitions nor intraexcitonic transitions within the green series.

In order to deduce the relation between induced $1s\rightarrow np$ absorption within the yellow series and the $1s$ exciton density we first need the corresponding dipole matrix elements which will be derived using a modified hydrogen model. For the sake of clarity we point out that within the scope of our contribution the term Bohr radius means just the parameter a_B which usually occurs in the hydrogen wave functions.[39] The expression $\hat{r}=n^2\cdot a_B$ which is also referred to as Bohr radius by some authors is actually the maximum of the probability density $W(r)dr$ for a given main quantum number n.

Unlike the hydrogen atom where a_B is identical for all states the situation for the yellow series excitons is different: while the np excitons share the same Bohr radius of $a_{B,np} \approx 1.1$ nm, which can be deduced[34] from their Rydberg energy and reduced mass, for $1s$ excitons the enhanced binding energy results in a distinctly smaller value[3] of $a_{B,1s} \approx 0.53$ nm. Since the dipole matrix element (e.g., in z-polarization) for a $1s\rightarrow np$ transition is given by

$$\mathbf{E}\parallel\mathbf{e}_z{:}\mu_{np1s,z}=\langle n,1,0|e\cdot r\cdot\cos(\theta)|1,0,0\rangle, \tag{4}$$

it is considerably diminished because the smaller value of $a_{B,1s}$ reduces the overlap of $1s$ and np wave functions.

As the matrix element calculated via Eq. (4) does not act on spin we can separate the transitions within the spin *para*- and *ortho* states according to Fig. 4. Since we use an unpolarized probe beam and since the excited electron-hole pairs are randomized during their relaxation, the same matrix element and transition probability according to (5) apply for both multitudes of Fig. 4:

$$|\mu_{2p1s}|^2_{para}=|\mu_{2p1s}|^2_{ortho}=6.8\cdot 10^{-58}\ \mathrm{C}^2\,\mathrm{m}^2. \tag{5}$$

Thereby the matrix elements μ_{2p1s} follow from Table II by using standard hydrogen wave functions,[39] indeed with $a_{B,1s}\neq a_{B,np}$. For $1s\rightarrow 2p$ and $1s\rightarrow 3p$ transitions the resulting matrix elements are summarized in Table II.

In order to calculate induced absorption due to a transition i with matrix element μ_i, we apply a Lorentz oscillator model. Although the real transition lineshape deviates from a Lorentzian, this does not cause an additional error since the

TABLE II. Dipole matrix elements for $1s \rightarrow 2p$ and $1s \rightarrow 3p$ transitions including a comparison to the standard hydrogen formulas where e is the elementary charge. Values are rounded to the first decimal place. Second column: matrix elements in z-polarization for the hydrogen atom using the same Bohr radius a_B for all states. Third column: matrix elements in z-polarization for yellow series excitons in Cu_2O with $a_{B,1s}=0.53$ nm and $a_{B,np}=1.1$ nm. Note that for the borderline case $a_{B,1s}=a_{B,np}=a_B$ these expressions reduce to the simple hydrogen formulas of the second column.

$1s \rightarrow np$	$\mu_{np1s,z}$ (H-atom)	$\mu_{np1s,z}$ (yellow series excitons)
$1s \rightarrow 2p$	$\frac{2^{15/2}}{3^5} \cdot a_B \cdot e$	$\frac{2^{15/2} \cdot a_{B,1s}^{7/2} \cdot a_{B,np}^{5/2}}{(2 \cdot a_{B,np} + a_{B,1s})^5} \cdot e \approx 2.6 \cdot 10^{-29}$ C m
$1s \rightarrow 3p$	$\frac{3^3}{2^{13/2}} \cdot a_B \cdot e$	$\frac{2(a_{B,1s}a_{B,np})^{7/2} - a_{B,1s}^{9/2}a_{B,np}^{5/2}}{(a_{B,1s} + 3a_{B,np})^6} \cdot 2^{-11/2} \cdot 3^3 \cdot e \approx 1.4 \cdot 10^{-29}$ C m

final density calibration will only contain the integrated area of induced absorption. The dimensionless oscillator strength depends on μ_i via[45]

$$f_i = \frac{2mE_i}{\hbar^2 e^2} \cdot |\mu_i|^2 \tag{6}$$

with m the reduced mass and E_i the transition energy. Let $\tilde{\varepsilon}(E)$ be the complex dielectric function where $E=\hbar\omega$ is the infrared photon energy, then the dielectric function with simultaneous cw laser excitation is

$$\tilde{\varepsilon}^*(E) = \tilde{\varepsilon}(E) + \sum_i \chi_i^*(E). \tag{7}$$

The transition induced susceptibility χ_i^* is given by[45]

$$\chi_i^*(E) = \frac{n_{1s}\hbar^2 e^2}{m\varepsilon_0} \cdot \frac{f_i}{E_i^2 - E^2 - i\hbar\Gamma E}, \tag{8}$$

where Γ is the damping and n_{1s} is either the density of $1s$ *para*-excitons or $1s$ *ortho*-excitons, depending on the transition type. Induced absorption is solely caused by the additional imaginary part

$$\tilde{\varepsilon}_2^* = \mathrm{Im}[\tilde{\varepsilon}^*(E) - \tilde{\varepsilon}(E)] = \mathrm{Im}\left(\sum_i \chi_i^*\right) \tag{9}$$

and thus for one particular transition it can be written as[34,45]

$$\alpha_{\mathrm{ind},i}(E) = \frac{\tilde{\varepsilon}_{2,i}^*(E) \cdot E}{\hbar c \cdot n(E)} \approx \frac{\mathrm{Im}[\chi_i^*(E)] \cdot E}{\hbar c \cdot \sqrt{\varepsilon_B}}, \tag{10}$$

where c is the velocity of light. The index of refraction $n(E)$ was already approximated by $\sqrt{\varepsilon_B}$ since even in the vicinity of MIR absorption band 2 the condition $\mathrm{Re}[\tilde{\varepsilon}^*(E)] \gg \mathrm{Im}[\tilde{\varepsilon}^*(E)]$ is fulfilled. Inserting Eqs. (6) and (8), for $\hbar\Gamma \ll E_i$ which is easily valid Eq. (10) results in

$$\alpha_{\mathrm{ind},i}(E) \approx \frac{2E_i n_{1s}|\mu_i|^2}{\hbar\sqrt{\varepsilon_B}\varepsilon_0 c} \cdot \frac{\hbar\Gamma/4}{(E_i - E)^2 + (\hbar\Gamma/2)^2}. \tag{11}$$

The ratio on the right-hand side describes a normalized Lorentzian the integrated area of which is $\pi/2$, independent from Γ and E_i. Finally the integration of Eq. (11) yields the searched connection between the density of $1s$ excitons and the area of induced absorption A_i,

$$n_{1s} = \frac{\hbar\varepsilon_0 c\sqrt{\varepsilon_B}A_i}{\pi|\mu_i|^2 E_i} \text{ with } A_i = \int \alpha_{\mathrm{ind},i}(E) \cdot dE. \tag{12}$$

Once a transition is identified, e.g., by its transition energy and temperature dependence, the $1s$ density can be calibrated by inserting the corresponding $|\mu_i|^2$ from Table II and the integrated induced absorption into Eq. (12).

B. Assignment of the observed transition

Figure 5 shows two typical pump-probe spectra for excitation in the phonon assisted absorption continuum of the $1s$ *ortho*-exciton which was our preferred excitation condition. Since in this case the temperature dependent absorption length ranges between 100 and 300 μm which is comparable to the sample thickness, and the excitons are additionally distributed by diffusion,[12] the resulting density profile should be relatively uniform.

We find a clear signal at the nominal $1s$ *para* $\rightarrow 2p$ *para* transition energy which broadens, becomes weaker and slightly shifts to the blue with increasing temperature. With regard to transition energy, a $1s$ *ortho* $\rightarrow 3p$ *ortho* transition would match as well, however this can be excluded: in this case we should also observe the $1s$ *ortho* $\rightarrow 2p$ *ortho* transi-

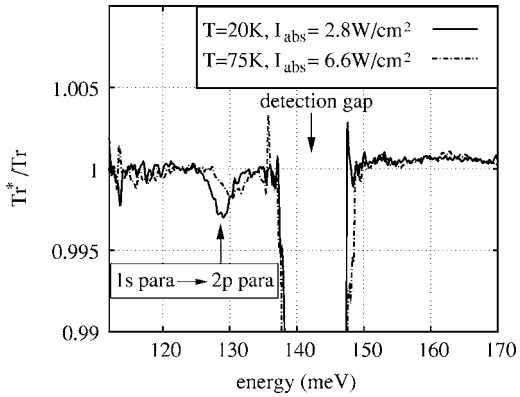

FIG. 5. Ratio of transmission spectra with (Tr^*) and without (Tr) cw laser excitation [$E_\gamma \approx 2.06$ eV, 650 μm (111) sample] for two temperatures. Note that the absorbed excitation density I_{abs} is considerably higher for $T=75$ K. The detection gap arises from MIR absorption band 2 (see Sec. III D).

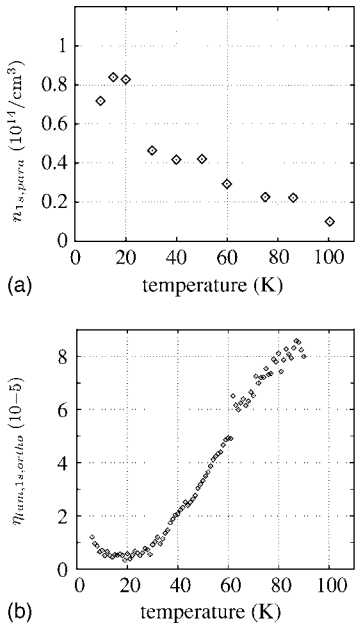

FIG. 6. (a) Temperature dependent density of 1*s para*-excitons, extracted from the area of induced absorption via Eq. (12) (650 μm sample). In order to create 1*s ortho*-excitons with constant excess energy, the laser was redshifted parallel to the 1*s ortho*-exciton with increasing temperature from 2.06 eV at 10 K to 2.047 eV at 100 K. The indicated densities are normalized to an absorbed photon flux density of $\approx 1.8 \cdot 10^{19}/(\mathrm{cm}^2\,\mathrm{s})$ corresponding to $\approx 6.0\ \mathrm{W/cm}^2$ for $E_\gamma = 2.06$ eV. (b) External photoluminescence quantum efficiency of the 1*s ortho*-exciton (data from Ref. 8). Since phonon assisted emission clearly dominates the PL spectrum, the quantum efficiency directly reflects the temperature dependence of the 1*s ortho* population.

tion at ≈ 116 meV which should be more than three times stronger (see Table II). Although most of the data that we present stems from the 650 μm sample, we point out that the signal was reproduced on four different samples. In the case of the thinnest sample ($d \approx 210$ μm), it was distinctly weaker, most likely due to enhanced surface recombination.

The interpretation in terms of a 1*s para* $\rightarrow$ 2*p para* transition is strongly confirmed by the temperature dependent area of induced absorption

$$A = \int \alpha_{\mathrm{ind}}(E) \cdot dE = \frac{1}{d} \cdot \int \ln \frac{\mathrm{Tr}(E)}{\mathrm{Tr}^*(E)} \cdot dE, \qquad (13)$$

where Tr^* (Tr) is the transmission spectrum with (without) laser excitation and d is the sample thickness. Using $|\mu_{2p1s}|^2$ from Table II the calibration [Eq. (12)] results in the temperature dependent 1*s para* density represented in Fig. 6(a) which is just complementary to the corresponding 1*s ortho* population [Fig. 6(b)]. In fact this is exactly what one would expect for the 1*s para*-exciton: since an interconversion mechanism[9] between the two 1*s* species is generally accepted to explain the temperature dependent 1*s ortho* population,[8] our findings fit well into that picture. Even the slight maximum of the 1*s para* density at $T \approx 15$ K coincides with the corresponding minimum of the 1*s ortho* population.

If 1*s ortho* and *para*-excitons are in mutual thermal equilibrium—which occurs according to Fig. 6 beyond 30–40 K—their densities should be already comparable at $T = 100$ K. However, we do not observe a 1*s ortho* $\rightarrow$ 2*p ortho* transition within the whole temperature range between 10 and 100 K within the experimental error. Admittedly the signal to noise ratio at the nominal transition energy (≈ 116 meV) is considerably smaller and decreases with increasing temperature. Thus we cannot draw a definite conclusion concerning the question if there are 1*s ortho*-excitons in a density appropriate to thermal equilibrium and the 1*s para*-exciton density of Fig. 6(a) above 40 K. While many authors assume thermal equilibrium between 1*s para*- and *ortho*-excitons at higher temperatures $\gtrsim 30$ K, there are also reports that the *ortho*-exciton density may remain below its equilibrium value due to its shorter lifetime.[46] Furthermore deviations of the matrix elements from the hydrogenlike values of Table II may come into play.

An estimation of the 1*s para* lifetime τ_p does not only require the density but also the generation rate $G_{1s,para}$ of 1*s para*-excitons. We know the absorbed photon flux P_γ quite precisely since all given values are carefully corrected for losses at the cryostat windows as well as for reflection and transmission of the sample. On the other hand, the fact that we initially excite 1*s ortho*-excitons with considerable excess energy demands further considerations. First, not each absorbed photon necessarily creates one *ortho*-exciton. A rapid capture into deep centers[47] or a fast surface recombination will reduce the creation efficiency. Therefore it seems advisable to introduce a phenomenological creation efficiency $\sigma_{1s,ortho}$. Secondly, only the temperature dependent fraction C_p of 1*s ortho*-excitons is converted into 1*s para*-excitons. Therefore the relation between 1*s para* density and lifetime for cw excitation can be approached as

$$n_{1s,para} \cdot V_{\mathrm{exc}} \approx G_{1s,para} \cdot \tau_p = \sigma_{1s,ortho} \cdot C_p \cdot P_\gamma \cdot \tau_p, \quad (14)$$

where P_γ and $G_{1s,para}$ are measured in units of s^{-1} and V_{exc} is the volume of the cloud of 1*s para*-excitons. As we are interested in the maximum lifetime τ_P this estimation will be accomplished for $T = 15$ K where the 1*s para* density exhibits its maximum. Using conversion and impurity loss rates from Ref. 48 we obtain $C_p(15\ \mathrm{K}) \approx 0.8$, implying that the majority of *ortho*-excitons is converted into *para*-excitons. Inserting this value as well as the corresponding numbers for P_γ and $n_{1s,para}$ yields

$$\tau_p(15\ \mathrm{K}) \approx 0.4\ \mu\mathrm{s}/\sigma_{1s,ortho},$$

$$\mathrm{resp.}\ \tau_p'(15\ \mathrm{K}) \approx 1.5\ \mu\mathrm{s}/\sigma_{1s,ortho}, \qquad (15)$$

where τ_p and τ_P' consider the two borderline cases for the adopted volume V_{exc}. Since pump and probe spot where congruent (diameter=2 mm), τ_p' allows also for lateral diffusion of *para*-excitons outside the probed sample volume using a diffusion length[12] of 1 mm, while τ_p is calculated for negligible lateral diffusion.

Because Eq. (15) still contains the creation efficiency of 1*s ortho*-excitons, the numbers themselves can be considered as lower limit of the 1 *s para* lifetime corresponding to the case $\sigma_{1s,ortho} = 1$. As already suggested in Sec. I we can estimate the creation efficiency of 1*s para*-excitons using the

data from Ref. 21 which will be done in the following for $T=4.2$ K. The following considerations are only valid, if the samples used here and in Ref. 21 are comparable concerning trap- or defect densities, etc. Despite these limitations, the following comparison may give interesting information. For the given sample thickness of 170 μm in Ref. 21 and the applied excitation energy of 2.066 eV which is almost identical to ours we find that approximtely 50% of the 2 μJ pulse used in Ref. 21 are absorbed. Using the quoted excitation area of $1.3\cdot10^5(\mu\text{m})^2$, the unrealistic scenario where each photon finally creates one *para*-exciton would result in an average initial density $\hat{n}_{1s,para}\approx 1.4\cdot10^{17}$ cm^{-3}. On the other hand, we can apply our density calibration: 200 ps after the pulse we find from the data of Ref. 21 $n_{1s,ortho}=n_{1s,para}\approx 5.4\cdot10^{15}$ cm^{-3}. The areas of both $1s\rightarrow 2p$ transitions are comparable for this delay.

The creation efficiency $\sigma_{1s,para}$ of $1s$ *para*-excitons for excitation in the phonon assisted absorption continuum of the $1s$ *ortho*-exciton can now be estimated via $\sigma_{1s,para}\approx n_{1s,para}/\hat{n}_{1s,para}\approx 0.08$ at 15 K. Replacing $G_{1s,para}$ in Eq. (14) by $\sigma_{1s,para}\cdot P_\gamma$ yields $\sigma_{1s,ortho}=\sigma_{1s,para}/C_p$ which can in turn be inserted into Eq. (15). Finally we obtain by combining our results for cw excitation with the creation efficiency extracted from Ref. 21

$$\tau_p\approx 4\ \mu\text{s}, \quad \text{respectively,} \quad \tau_p'\approx 16\ \mu\text{s}. \tag{16}$$

While this result is in good agreement with $\tau_p\approx 13$ μs from Ref. 11, it is three orders of magnitude larger than the lifetime published in Ref. 10 and two orders of magnitude smaller than that one published in Ref. 12.

If the above condition, that the samples are of comparable quality is valid, this finding may have consequences on the interpretation of the data in various publications. Possibly long time transport properties[12] are influenced at later times more by a diffusively or ballistically propagating cloud of phonons rather than excitons. See in this context also Refs. 49–51 and references therein.

C. Line shape analysis

The theoretical line shape of induced absorption neither depends on the particular involved $1s$ species nor on main quantum number and spin of the final p-state. Therefore we consider two generalized states $1s$ and np as depicted in Fig. 7 and the result can later be applied to a particular transition by using the corresponding parameters. Let $\mathbf{q}$ be the wave vector of the infrared photon, then the approximation $\mathbf{k}+\mathbf{q}\approx\mathbf{k}$ is well justified implying perpendicular transitions with regard to Fig. 7. Since we are dealing with the situation $m_{1s}>m_{np}$ the energy gap $E_{np1s}(k)$ between $1s$ and np state increases with increasing k,

$$E_{np1s}(k)=\Delta E_0+\frac{\hbar^2k^2}{2}\cdot\left(\frac{1}{m_{np}}-\frac{1}{m_{1s}}\right). \tag{17}$$

Preliminary disregarding homogeneous broadening which will be considered afterwards, the transition rate W_{np1s} can directly be written by applying Fermi's Golden Rule,

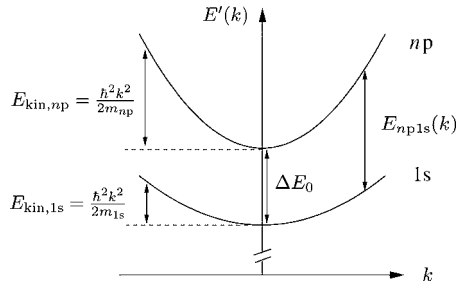

FIG. 7. Dispersions of generalized $1s$ and np states including the notations which are used to deduce the theoretical line shape of induced $1s\rightarrow np$ absorption. Since the calculation will be done on the energy scale E of the infrared photons which have their k-dependent energetical zero point in the $1s$ dispersion, the "old" energy scale is denoted by $E'(k)$.

$$W_{np1s}=\frac{2\pi}{\hbar}\int|\mu_i|^2f_{1s}(\mathbf{k})[1+f_{np}(\mathbf{k})]f_\gamma(\mathbf{q})\cdot\delta[E_{np1s}(\mathbf{k})-\hbar c\mathbf{q}]\cdot d^3\mathbf{k}. \tag{18}$$

Thereby μ_i is the transition matrix element while f_{1s}, f_{np}, and f_γ are the distribution functions of $1s$ excitons, np excitons and of the infrared photons. From Eq. (18) we will now derive the line shape $\alpha_{\text{ind}}(E)$ of induced absorption which is based on the following assumptions:

(1) The matrix element μ_i is k-independent.

(2) Since dipole transitions in a cubic lattice are direction independent[34] it follows $d^3\mathbf{k}=4\pi k^2dk$.

(3) The population of the np level can be neglected.

Since f_γ cancels [see Eq. (13)] this approach yields

$$\alpha_{\text{ind}}(E)\propto\int k^2f_{1s}(k)\,\delta[E_{np1s}(k)-E]\cdot dk, \tag{19}$$

where we already introduced the new energy scale $E=\hbar c|\mathbf{q}|$ of the infrared probe beam. Equation (19) can be transferred into an integral over E_{np1s} by using Eq. (17),

$$\alpha_{\text{ind}}(E)\propto\int f_{1s}(E_{np1s})\cdot\sqrt{E_{np1s}-\Delta E_0}\cdot\delta(E_{np1s}-E)\cdot dE_{np1s}. \tag{20}$$

Because the maximum $1s$ exciton density is in the order of 10^{14} cm^{-3} the Boltzmann approximation is valid for a thermal distribution within the $1s$ band, resulting in

$$\alpha_{\text{ind}}(E)\propto\sqrt{E-\Delta E_0}\cdot\exp\left[\frac{-(E-\Delta E_0)}{\left(\frac{m_{1s}}{m_{np}}-1\right)\cdot k_BT}\right]. \tag{21}$$

As already suggested by Fig. 7, with increasing temperature $\alpha_{\text{ind}}(E)$ broadens on its high energy side. In addition, the more m_{1s} exceeds m_{np}, the broader the line shape will become. On the other hand, for the borderline case $m_{1s}=m_{np}$ Eq. (21) reduces to a delta function at $E=\Delta E_0$. Higher exciton densities require to insert a Bose distribution into Eq. (20) which will not be carried out here. Qualitatively however it is clear that when the chemical potential approaches zero, the line shape will increasingly narrow. Detailed line

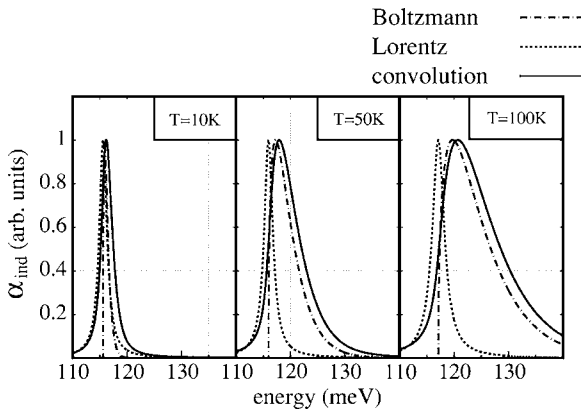

FIG. 8. Theoretical line shape of induced absorption for a 1*s ortho*→2*p ortho* transition. The dashed-dotted line corresponds to Eq. (21), while the solid line shows the numerical convolution of Eq. (21) with a Lorentzian (dotted line) using the temperature dependent width of the 2*p ortho* Γ_4^- state.

shape considerations in the case of BEC can be found in Ref. 17.

In order to obtain a realistic line shape we also have to allow for homogeneous broadening. Depending on temperature and sample quality the homogeneous linewidth of the 1*s ortho*-exciton[52–54] ranges between 0.4 and 100 μeV and should be comparable for the 1*s para*-exciton. The corresponding transition broadening can be neglected for both of the 1*s* species as already the linewidth given by Eq. (21) is in the order of k_BT. In the case of *np* excitons this is no more true: using linear absorption data, for the 2*p ortho* Γ_4^- state we find a homogeneous linewidth of $\approx$1.7 meV at $T=10$ K increasing to $\approx$2.6 meV at $T=100$ K. Since the dominant dephasing mechanism is phonon scattering which should not be too sensitive to spin, we expect homogeneous broadening of a particular *np* state to be comparable with the corresponding *np ortho* Γ_4^- state. The influence of homogeneous broadening is taken into account by the convolution of Eq. (21) with a Lorentzian (the width given by the homogeneous linewidth of the according *np* exciton). Simulated induced absorption spectra can be seen in Fig. 8 where we chose a 1*s ortho*→2*p ortho* transition because in this case all parameters are known from experiment.

Figure 9 shows spectra of induced 1*s para*→2*p para* absorption for different temperatures. The spectra can be well fitted with Eq. (21). The effective mass of the 1*s para*-exciton extracted from the fit in Fig. 9 is in the temperature interval from 10 to 45 K $(2.20\pm0.1)m_0$, with a trend to decrease with increasing temperature to values around $1.86m_0$ at 100 K as shown in Fig. 10.

Different interpretations are possible for this finding (deviations from Boltzmann statistics can be ruled out in the considered temperature and density regimes): (i) obviously a decreasing effective mass with increasing T or at least with increasing **k** and kinetic energy of the 1*s para*-excitons [see Fig. 10(a)]; (ii) a decrease of the matrix element with increasing **k**, caused e.g., by a **k**-dependent *para-ortho* mixing (see below); (iii) a weaker T-dependence of the homogeneous broadening of 2*p para*-excitons compared to the 2*p ortho*-excitons. Although the temperature dependent linewidth reported in Ref. 21 is almost identical to our results, the authors of Ref. 21 state that they can well fit the line shape by using $m_{1s,para}=2.7m_0$ and assuming a Boltzmann distribution, unfortunately without going into detail concerning the applied fit formula. At this point we disagree, e.g., for $T=70$ K the halfwidth indicated in Fig. 5 of Ref. 21 ranges between 3 and 4 meV which is consistent with our results, but distinctly below the expected width of 8 meV. Even a complete neglect of homogeneous broadening would still result in a width of 7 meV.

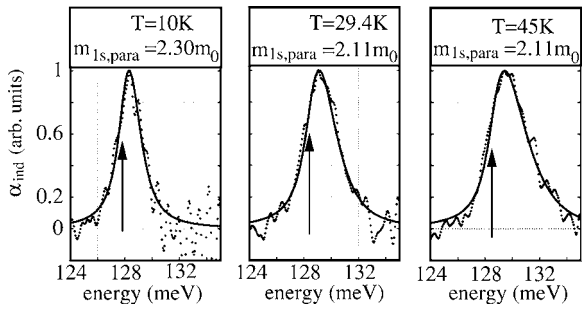

FIG. 9. Normalized induced absorption due to a 1*s para*→2*p para* transition for excitation in the phonon assisted absorption continuum where the absorbed excitation density was $\approx$6 W/cm^2. The indicated fit (solid line) was accomplished by using the homogeneous linewidth of the 2*p ortho* Γ_4^- state and fixing the exciton temperature to the lattice temperature. The effective mass $m_{1s,para}$ as well as the transition energy ΔE_0 (indicated by arrows) where used as fit parameters.

An effective mass of the 1*s para*-exciton noteworthy smaller than $2.7m_0$ might have interesting consequences. Since exchange interaction and the effective mass of the 1*s ortho*-exciton exhibit a characteristic **k**-dependence[52,53] with values reaching $5.4m_0$, there might be particular directions in **k**-space where 1*s ortho* and 1*s para* dispersion cross at relatively small wave vectors. Also in the case of an avoided crossing along with the mixing of both states the gap between the dispersions might be significantly reduced. Both

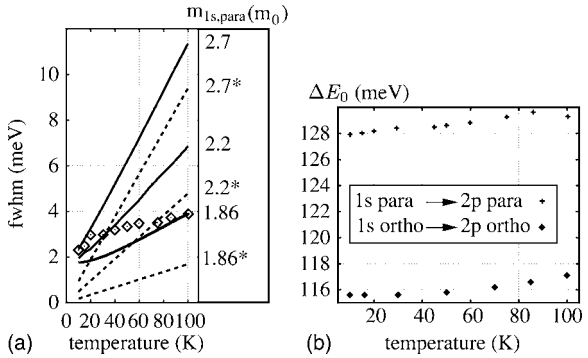

FIG. 10. (a) Observed halfwidth of the 1*s para*→2*p para* transition (data points) in comparison to the expected halfwidth (solid lines) for different effective masses of the 1*s para*-exciton. The dashed lines are calculated for neglected homogeneous broadening of the 2*p para* state. (b) Observed 1*s para*→2*p para* transition energy as a function of temperature compared to the nominal 1*s ortho*→2*p ortho* transition energy extracted from linear absorption and photoluminescence.

cases could give rise to an additional efficient 1*s ortho* to 1*s para* conversion channel which might explain the extremely different values for the Auger coefficient of the 1*s ortho*-exciton.[12,55–57] Results as in Ref. 55 where the authors interpret the sublinear increase of the *ortho*-excitons luminescence intensity with increasing excitation power in terms of Auger recombination, could then be alternatively explained. With increasing density the effective temperature of the 1*s ortho*-excitons can be considerably higher than the lattice or bath temperature, e.g., due to inelastic exciton-exciton scattering. This is an effect frequently observed under high excitation.[34] The fraction of 1*s ortho*-excitons with a sufficiently large wave vector might then be converted into 1*s para*-excitons and would not contribute to photoluminescence anymore. An apparent increase of the Auger rate with the lattice temperature would find a simple interpretation via this conversion process. Measurements as those in Ref. 21 with different excitation fluences could contribute independently to the clarification of the controversy on the value of the Auger coefficient in Cu_2O.

While the *np ortho* Γ_4^- states shift parallel to the band gap with increasing temperature, linear absorption and photoluminescence data reveal that the 1*s ortho*-excitons binding energy slightly increases by $\approx$1.5 meV from 10 to 100 K. Consequently, the nominal 1*s ortho*$\rightarrow$2*p ortho* transition energy shown in Fig. 10(b) shifts to the blue as well. Since the 1 *s ortho*$\leftrightarrow$1*s para* splitting at the Γ-point is expected to be temperature independent, the fact that the extracted 1*s para*$\rightarrow$2*p para* transition energy [see Fig. 10(b)] shows a similar blueshift is a further independent confirmation that our assignment of the transition is correct. Due to the temperature dependent signal to noise ratio the 1*s para*$\rightarrow$2*p para* transition energy can be extracted most accurately in the low temperature range between 10 and 30 K where it is approximately 300 μeV above the nominal transition energy of 127.6 meV. However this small deviation does not mandatory imply a 2*p ortho*$\leftrightarrow$2*p para* splitting of 300 μeV but might also be related to the experimental error bar.

D. Excitation dependent measurements

Intensity dependent measurements yield an approximately linear increase of the 1*s para* density with excitation density and thus the absence of a notable Auger effect for the applied excitation conditions (see Fig. 11). However due to the moderate densities we can not take sides concerning the mentioned controversy about the Auger effect. The Auger coefficients published so far (see, e.g., Refs. 55–57) refer to the 1*s ortho*-exciton whereby the largest value is by far $A \approx 10^{-16}$ cm^3/ns from Ref. 55. This results with $n_P \approx 10^{14}$ cm^{-3} [Fig. 6(a)] in an effective decay time $(An_P)^{-1} \approx 0.1$ μs which is hardly compatible with the data of Ref. 15. However, the authors of Ref. 55 themselves concede that the Auger effect might be considerably smaller for 1*s para*-excitons. Therefore our data is not necessarily contradictory to the results of Ref. 55.

We also carried out measurements comparable to PLE (Fig. 12): starting at 2.06 eV the excitation energy was gradually redshifted along the phonon assisted absorption

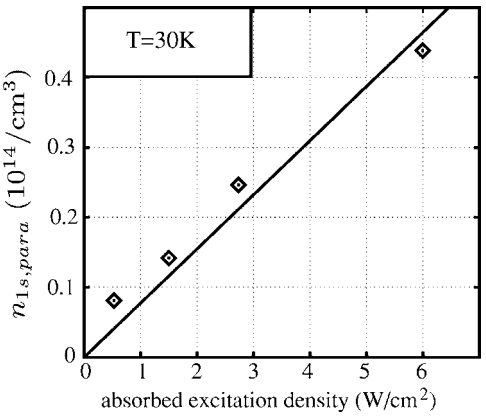

FIG. 11. Density of 1*s para*-excitons as a function of absorbed excitation density for excitation in the phonon assisted absorption continuum at $E_\gamma \approx 2.06$ eV [650 μm (111) sample].

edge. The increase of normalized induced absorption with decreasing excitation energy following from Figs. 12(a) and 12(b) above $\hbar\omega_{\mathrm{exc}}=2.05$ eV allows at least three different interpretations. First, the data could mirror the excitation dependent creation efficiency $\sigma_{1s,ortho}$ of 1*s ortho*-excitons. Second, $\sigma_{1s,ortho}$ might be approximately constant but the 1*s ortho*- to *para*-conversion could depend on excitation energy. Third, the fraction of excitons diffusing out of the probed sample volume might increase with increasing excess energy.

Measurements with resonant excitation of the 1*s ortho*-exciton where accomplished as well, indeed involving additional experimental problems. As long as the laser (FWHM ≈ 200 μeV) is slightly detuned against the 1*s ortho*-exciton quadrupole absorption line, the sample is neither excited nor heated at all. Tuning the laser into resonance results in a suddenly starting heat creation which in turn induces a redshift of the 1*s ortho*-exciton. This interplay has been used to obtain induced absorptive optical bistability.[34,58] It makes the interplay between excitation and temperature control a hard task.

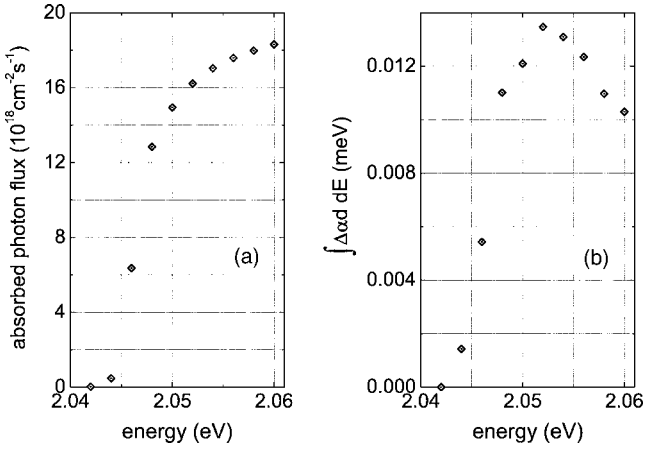

FIG. 12. Pump-probe results for different excitation energies in the phonon assisted absorption continuum [650 μm (111) sample, $T=30$ K]. (a) Absorbed laser photon flux density in the area of the phonon assisted absorption edge. (b) Corresponding integrated area of induced 1*s para*$\rightarrow$2*p para* optical density $\Delta\alpha d$.

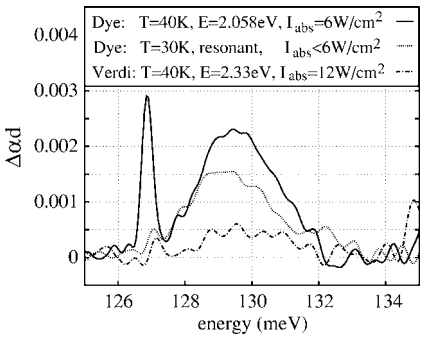

FIG. 13. 1*s para*→2*p para* transition for different excitation conditions [700 μm (100) sample]. Resonant excitation corresponds to an excitation energy of approximately 2.032 eV; in this case the given excitation density is only an upper boundary.

Figure 13 shows a comparison of pump-probe spectra in the case of phonon assisted, resonant and Verdi excitation. The fact that for resonant excitation the area of induced absorption is still comparable to phonon assisted excitation although the absorbed excitation density should be considerably smaller might imply that $\sigma_{1s,ortho}$ tends to unity in the resonant case. Furthermore Fig. 13 implies that excitation above the band gap is approximately one order of magnitude less efficient concerning the final creation of 1*s para*-excitons compared to phonon assisted excitation. This might be either explained by a further decrease of $\sigma_{1s,ortho}$ with increasing excitation energy or by enhanced surface recombination due to the reduced absorption length of the pump in the order of 10 μm.

As a last point we want to turn to the narrow peak at approximately 127 meV (Fig. 13). Although the observed signal is quite similar to the expected one in the case of BEC,[17] we consider this possibility to be highly unlikely. An estimation yields that reaching the critical density[59] which is in the order of $10^{18}/\mathrm{cm}^3$ at $T=40$ K would require a lifetime of the 1*s para*-exciton in the order of 100 ms. Actually narrow peaks as the one discussed appeared in several measurements.[20] While the main signal of induced absorption was consistent and reproducible, the energetic position and strength of the narrow peaks depended on sample, sample position, temperature, and excitation conditions. In our opinion these peaks, including partly our older results from Ref. 20, can be assigned to intraexcitonic transitions of impurity bound excitons. This interpretation would also be consistent with experiments which are related to our work but in an early stage[13] where a similar signal as the mentioned peak in Fig. 13 is observed. Though the authors themselves interpret their data as a 1*s para*→2*p para* transition of free excitons, we seriously doubt this statement. The reported decay time of 14 ms, the saturation of the signal with increasing excitation density at rather low pump levels, as well as the linewidth considerably below 1 meV are much more consistent with transitions of impurity bound excitons than with the interpretation given in Ref. 13.

V. CONCLUSION AND OUTLOOK

The observation of the excitonic Lyman series in absorption gives valuable information on exciton states, which are difficult to reach by other optical means. An extension of such investigation would be the search for $2p \rightarrow 1s$ luminescence, e.g., under resonant $2p$ excitation, which is in Cu_2O much more efficient than 1*s* excitation.

ACKNOWLEDGMENTS

We thank the Deutsche Forschungsgemeinschaft for financial support. Furthermore, we thank Dr. G. Kavoulakis (Lund/Sweden), Professor Dr. H. Stolz (Rostock/Germany) and Professor Dr. V. Burlakov (Oxford/UK) for fruitful discussions.

Note added in proof: In a recent publication [M. Kubouchi, K. Yoshioka, R. Shimano, A. Mysyrowicz, and M. Kuwata-Gonokami, Phys. Rev. Lett. **94**, 016403 (2005)] additional low temperature data to Ref. 21 have been published, showing among others the relaxation from 1*s ortho* to 1*s para* excitons on time scales around 1 ns. Unfortunately, the time interval covered therein is still too short to answer the questions of the lifetime of *para*-excitons discussed here in Sec. IV B.

*This work has been partly presented at the spring meeting of the German Physical Society in 2004 [Verhandlungen DPG (VI) 39,2/HL12.17 (2004)] and at ICSCE, Pittsburgh 2004 [Solid State Commun. **134**, 155 (2005)].

[1] A. Jolk and C. Klingshirn, Phys. Status Solidi B **206**, 841 (1998), and references therein.
[2] R. J. Elliott, Phys. Rev. **108**, 1384 (1957).
[3] G. M. Kavoulakis, Y. C. Chang, and G. Baym, Phys. Rev. B **55**, 7593 (1997).
[4] R. Wyckoff, *Crystal Structures* (Wiley, New York, 1965), Vol. 2.
[5] O. Madelung and M. Schulz, *Landolt-Börnstein New Series: Group III Semiconductors* (Springer, Berlin, Heidelberg, New York, Tokyo, 1983), Vol. 17e.
[6] J. Hodby, T. Jenkins, H. Tamura, and D. Trivich, J. Phys. C **9**, 1429 (1976).
[7] N. Caswell, J. Weiner, and P. Yu, Solid State Commun. **40**, 843 (1981).
[8] M. Jörger, M. Schmidt, A. Jolk, R. Westphäling, and C. Klingshirn, Phys. Rev. B **64**, 113204 (2001).
[9] D. W. Snoke, D. P. Trauernicht, and J. P. Wolfe, Phys. Rev. B **41**, 5266 (1990).
[10] S. Denev and D. W. Snoke, Phys. Rev. B **65**, 085211 (2002).
[11] A. Mysyrowicz, D. Hulin, and A. Antonetti, Phys. Rev. Lett. **43**, 1123 (1979).
[12] A. Jolk, M. Jörger, and C. Klingshirn, Phys. Rev. B **65**, 245209 (2002).
[13] K. Karpinska, P. van Loosdrecht, I. Handayani, and A. Revcolevschi, J. Lumin. **112**, 17 (2005).

[14] D. Hulin, A. Mysyrowicz, and C. Benortala Guillaume, Phys. Rev. Lett. **45**, 1970 (1980).
[15] D. W. Snoke, J. P. Wolfe, and A. Mysyrowicz, Phys. Rev. B **41**, 11171 (1990).
[16] E. Fortin, S. Fafard, and A. Mysyrowicz, Phys. Rev. Lett. **70**, 3951 (1993).
[17] K. Johnsen and G. M. Kavoulakis, Phys. Rev. Lett. **86**, 858 (2001).
[18] D. Labrie, M. L. W. Thewalt, I. J. Booth, and G. Kirczenow, Phys. Rev. Lett. **61**, 1882 (1988).
[19] T. Timusk, Phys. Rev. B **13**, 271 (1975).
[20] M. Jörger, E. Tsitsishvili, T. Fleck, and C. Klingshirn, Phys. Status Solidi B **238**, 470 (2003); M. Göppert, R. Becker, C. Maier, M. Jöerger, A. Jolk and C. Klingshirn, Proc. EXCON, edited by K. Cho and A. Matsui, Yamada Conf. L III (World Scientific, Singapore, 2000), p. 47.
[21] M. Kuwata-Gonokami, M. Kubouchi, R. Shimano, and A. Mysyrowicz, J. Phys. Soc. Jpn. **73**, 1065 (2004).
[22] M. M. Beg and S. M. Saphiro, Phys. Rev. B **13**, 1728 (1975).
[23] G. E. Kugel, C. Carabatos, and W. Kress, J. Phys. Colloq. **42**, C6 (1981).
[24] M. Ivanda, D. Waasmaier, A. Endriss, J. Ihringer, A. Kirfel, and W. Kiefer, J. Raman Spectrosc. **28**, 487 (1997).
[25] V. M. Agranovich, *Spectroscopy and Exciton Dynamics of Condensed Molecular Systems* (North-Holland, Amsterdam, 1983).
[26] M. Sparks and L. J. Sham, Phys. Rev. B **8**, 3037 (1973).
[27] J. S. Ziomek, J. Phys. Chem. Solids **43**, 1037 (1982).
[28] E. Madelung, *Landolt-Börnstein, New Series, Group III* (Springer-Verlag, Berlin, 1998), Vol. 41C.
[29] S. Ishizuka, S. Kato, Y. Okamoto, and K. Akimoto, Appl. Phys. Lett. **80**, 950 (2002).
[30] T. Ito and T. Masumi, J. Phys. Soc. Jpn. **66**, 2185 (1997).
[31] P. Dawson, M. M. Hargreave, and G. R. Wilkinson, J. Phys. Chem. Solids **34**, 2201 (1973).
[32] J. Reydellet, M. Balkanski, and D. Trivich, Phys. Status Solidi B **52**, 175 (1972).
[33] J. C. W. Taylor and F. Weichman, Phys. Rev. **185**, 1214 (1969).
[34] C. F. Klingshirn, *Semiconductor Optics*, 2nd ed. (Springer-Verlag, Berlin, 2005).
[35] V. M. Burlakov, M. Göppert, A. Jolk, A. Dinger, R. Becker, and C. Klingshirn, Phys. Lett. A **254**, 95 (1999).
[36] P. Y. Yu and Y. R. Shen, Phys. Rev. B **12**, 1377 (1975).
[37] P. Y. Yu and Y. R. Shen, Phys. Rev. B **17**, 4017 (1978).
[38] M. Shmiglyuk, A. Bobrysheva, and V. Pavlov, Phys. Status Solidi B **199**, 427 (1997).
[39] C. Cohen-Tannoudji, B. Diu, and F. Laloe, *Quantum Mechanics 2* (Wiley-Interscience, New York, 1996).
[40] D. Fröhlich, R. Kenklies, C. Uihlein, and C. Schwab, Phys. Rev. Lett. **43**, 1260 (1979).
[41] C. Uihlein, D. Fröhlich, and R. Kenklies, Phys. Rev. B **23**, 2731 (1981).
[42] T. Ueno, J. Phys. Soc. Jpn. **26**, 438 (1969).
[43] K. Karpinska, P. van Loosdrecht, D. van der Marel, and A. Revcolevschi, in Proceedings of the ICPS in Edinburgh, Institute of Physics conference series, edited by A. R. Long and J. H. Davies (Institute of Physics Publishing, Bristol, Philadelphia, 2002), CDROM, Vol. 171, p. 49.
[44] R. J. Elliott, Phys. Rev. **124**, 340 (1961).
[45] F. Wooten, *Optical Properties of Solids* (Academic, New York, 1972).
[46] G. M. Kavoulakis and A. Mysyrowicz, Phys. Rev. B **61**, 16619 (2000).
[47] R. G. Kaufman and R. T. Hawkins, J. Electrochem. Soc. **133**, 2652 (1986).
[48] J. Weiner, N. Caswell, P. Yu, and A. Mysyrowicz, Solid State Commun. **46**, 105 (1983).
[49] C. Klingshirn, T. Fleck, and M. Jörger, Phys. Status Solidi B **234**, 23 (2002).
[50] A. Mysyrowicz, P. Leblanc, and E. Fortin, Phys. Status Solidi B **239**, 257 (2003).
[51] C. Klingshirn, T. Fleck, and M. Jörger, Phys. Status Solidi B **239**, 459 (2003).
[52] G. Dasbach, D. Fröhlich, H. Stolz, R. Klieber, D. Suter, and M. Bayer, Phys. Rev. Lett. **91**, 107401 (2003).
[53] G. Dasbach, D. Fröhlich, H. Stolz, R. Klieber, D. Suter, and M. Bayer, Phys. Status Solidi B **238**, 541 (2003).
[54] F. Kreingold and V. Makarov, Fiz. Tverd. Tela (S.-Peterburg) **17**, 472 (1975).
[55] K. E. OHara, J. R. Gullingsrud, and J. P. Wolfe, Phys. Rev. B **60**, 10872 (1999).
[56] D. W. Snoke and J. P. Wolfe, Phys. Rev. B **42**, 7876 (1990).
[57] S. Denev and D. W. Snoke, Phys. Rev. B **65**, 085211 (2002).
[58] G. Dasbach, G. Baldassarri Hoger van Högersthal, D. Fröhlich, H. Stolz, and M. Bayer, Phys. Rev. B **70**, 121202(R) (2004).
[59] G. M. Kavoulakis, Phys. Rev. B **65**, 035204 (2001).